Environmental Science
Advances

ROYAL SOCIETY
OF CHEMISTRY

PAPER

View Article Online
View Journal

Cite this: DOI: 10.1039/d6va00039h

Synergistic interface engineering in ZnO@CNT catalysts: electronic modulation for switching peroxydisulfate activation toward a $^1O_2$-dominated non-radical pathway

Qian Zhou,[a] Qingsong Liu,[a] Chenglin Li,[b] Liu Yang,[a] Yu Xue,[a] Shengqiong Fang *[a] and Weiguang Lan*[c]

Received 21st January 2026
Accepted 17th March 2026

DOI: 10.1039/d6va00039h

rsc.li/esadvances

Currently, during peroxydisulfate (PDS) activation through Fenton-like reactions, transition metal catalysts face the problem of leaching, whereas carbonaceous materials pose challenges such as difficult recovery, insufficient stability, and less-than-ideal catalytic performance in peroxydisulfate systems. In response to these challenges, the novel composite catalyst (ZnO@CNT) was synthesized through a straightforward one-pot pyrolysis approach. This innovative material exhibits both superior catalytic activity and minimal cytotoxicity, enabling effective activation of peroxodisulfate (PDS) for the degradation of antibiotic sulfamethoxazole (93.56% removal within 30 min kinetic constant: 0.089 min^{-1}). Characterization and density functional theory (DFT) calculations confirmed that the synergistic coupling between ZnO nanoparticles and carbon nanotubes creates abundant active interfaces, thereby enhancing electron transfer and reactive oxygen species generation. Unlike traditional radical-based oxidation systems, mechanistic studies combining electron paramagnetic resonance (EPR) and quenching experiments have identified singlet oxygen ($^1O_2$) as the primary reactive species, which confers exceptional resistance to complex water matrices containing various interfering substances. Electrochemical analyses provide fundamental insights into the enhanced PDS activation mechanism, demonstrating that ZnO incorporation modulates the electronic structure of CNTs to favor $^1O_2$ generation. ZnO@CNT exhibits outstanding cycling stability and environmental safety, as verified by toxicity assessment of transformation products. This work not only develops an efficient metal–carbon hybrid catalyst, but also advances the fundamental understanding of non-radical oxidation pathways for sustainable water purification applications.

Environmental significance

Addressing antibiotic pollution requires advanced oxidation technologies that are both highly effective and environmentally compatible. Many current systems rely on radical species that are easily scavenged in complex real-world waters. We developed a novel nanocomposite that generates singlet oxygen, a potent yet selective oxidant, for degrading sulfamethoxazole without significant metal leaching. This work provides a fundamental advance in designing non-radical catalytic nanotechnologies. It demonstrates a pathway towards more efficient, stable, and safer water treatment processes, highlighting the role of rational material design in achieving sustainable environmental remediation.

1 Introduction

Sulfonamides (SAs) have become a global environmental and health concern due to their extensive use in clinical medicine, agriculture, aquaculture, and animal husbandry.[1] The persistence of these pharmaceuticals in aquatic environments poses threats to aquatic life and potential risks to human health. Sulfamethoxazole (SMX) is particularly resistant to biodegradation due to its stable molecular structure, leading to its accumulation in organisms.[2] Prolonged exposure to SMX in water environments can adversely affect human health and contribute to the proliferation of antibiotic-resistant bacteria and genes.[3] The widespread presence of SMX has driven the search for effective wastewater treatment technologies to mitigate its ecological impact.[4] The ubiquitous presence of SMX has prompted the exploration of effective wastewater treatment

---

[a] *College of Environment & Safety Engineering, Fuzhou University, Fuzhou, 350108, China. E-mail: haohaoxuexiazq@163.com; 695945583@qq.com; 18950132265@163.com; 435278571@qq.com; fsq@fzu.edu.cn*

[b] *Department of Chemistry & Faculty of Science, National University of Singapore, 119077, Singapore. E-mail: q919695560@gmail.com*

[c] *School of Future Membrane Technology, Fuzhou University, Fuzhou, Fujian, 350108, China. E-mail: Lanwg@suntar.com*

technologies to mitigate its ecological impact. Traditional techniques for SMX management, including evaporation, adsorption, and biological pretreatment, often demonstrate limited efficacy. Many wastewater treatment plants fail to effectively eliminate SMX, leading to its release into natural environments, exacerbating ecological risks. Therefore, developing more efficient SMX removal technologies is crucial for protecting aquatic life and maintaining ecological balance.

The efficacy of advanced oxidation processes (AOPs) in degrading pharmaceutical compounds such as SMX is attributed to their ability to generate reactive oxygen species (ROS), including hydroxyl radicals ($^{\bullet}OH$), sulfate radicals ($SO_4^{-\bullet}$), singlet oxygen ($^1O_2$), and superoxide radicals ($O_2^{-\bullet}$).[5] These ROS can efficiently degrade organic pollutants such as antibiotics. Peroxydisulfate (PDS) is a commonly used oxidant in AOPs, which can be activated through ultraviolet irradiation, heating, or the addition of acids, bases, and transition metals.[6–9] Notably, the transition metal-based catalysis approach represents the most practical and cost-efficient alternative, as it operates without dependence on external energy sources. Both homogeneous and heterogeneous transition metals can catalyze PDS, activating it into sulfate radicals *via* redox cycling.[10]

In recent years, precious metals including Ru, Pd, and Ag have demonstrated excellent PDS activation efficiencies due to their robust electron transfer capabilities.[11,12] Despite their advantages, the high cost and limited availability of precious metals have limited their widespread utility in various industries. Homogeneous transition metals, such as Co, Cu, and Ni, exhibit high catalytic activity in PDS activation. However, these dissolved metal ions pose a serious risk of secondary contamination as they are difficult to recycle and may persist in treated water, leading to potential ecotoxicity. Zinc (Zn)-based catalysts have emerged as a promising alternative due to their low toxicity and economy as well as environmental compatibility.[13–15] However, a major limitation of metal-based catalysts, including ZnO, is that they undergo agglomeration, which diminishes the active surface area and undermines the long-term catalytic performance. Aggregation of nanoparticles reduces the effective surface area and hinders mass transfer and active oxygen generation. Confining metal inside the nanochannels of carbon-based architectures creates highly active sites, which significantly enhances the degradation performance against organic pollutants. Therefore, the selection of suitable metal ion carriers can reduce the possibility of environmental contamination during the degradation process and enhance the stability of the catalyst. Among many carbon-based materials, carbon nanotubes (CNTs) stand out owing to their unique advantages.[16,17] First, CNTs have excellent PS adsorption and activation properties, which is largely conferred by their high specific surface area and the abundance of active sites.[18] Secondly, CNTs have inherent thermal and chemical stability.[19] As a metal carrier, carbon nanotubes can not only mitigate metal ion leaching to reduce secondary pollution, but also enhance electron transfer by dispersing active sites, thereby boosting catalytic performance.[20–23] Despite these advantages, the long-term stability of CNT-based catalysts remains a critical concern, as carbon materials are susceptible to oxidative degradation during prolonged AOP reactions. The reactive oxygen species (ROS) generated during PDS activation can attack the carbon framework, leading to structural damage, loss of active sites, and eventual catalyst deactivation. Recent literature has reported several effective strategies to mitigate CNT degradation and enhance long-term stability. These include heteroatom doping (*e.g.*, nitrogen or boron doping),[24,25] metal encapsulation or confinement strategies,[26,27] and surface functional group regulation.[28]

Zinc oxide (ZnO) is an effective PDS activator because its electronic structure promotes electron transfer to generate $SO_4^{-\bullet}$ and $^{\bullet}OH$. Upon immobilization on carbon-based materials, it suppresses metal ion leaching and facilitates electron transport, thereby improving the catalytic efficiency.[13,29] In particular, when ZnO is loaded on carbon nanotubes (CNTs), it has been shown to significantly increase the adsorption and activation efficiencies of PDS, which in turn improves the degradation of SMX. ZnO promotes the decomposition of PDS through surface catalysis to generate highly reactive radicals. Zn^{2+} ions on the surface of ZnO interact with PDS and accelerate the generation of free radicals. By loading ZnO onto carbon nanotubes, a ZnO@CNT catalyst can be synthesized, which not only improves the degradation efficiency of SMX, but also facilitates the separation and recycling from aqueous solution, reducing the risk of secondary pollution.

This study successfully fabricated a novel ZnO-loaded carbon nanotube (ZnO@CNT) catalyst by one-pot pyrolysis for water purification *via* the Fenton reaction. The CNT support in the resulting catalyst effectively confined zinc ions to minimize leaching, while enhancing the improved electron transport. Consequently, the incorporation of ZnO markedly boosted PDS activation, facilitating the production of reactive radicals that efficiently degraded SMX. In order to understand the structure, morphology and performance of the catalysts, we performed a series of characterization analyses on ZnO@CNT including Scanning Electron Microscopy (SEM), X-ray diffractometry (XRD), Raman spectroscopy and X-ray Photoelectron Spectroscopy (XPS) characterization, theoretical calculations and toxicity analyses to investigate the mechanism of SMX degradation by ZnO@CNT-activated PDS. We will provide an innovative solution for the study of Zn-loaded carbon material multiphase catalytic system activation of PDS for rapid removal of sulfamethoxazole.

2 Experimental part

2.1 Materials and characterization

The chemicals and reagents for the materials employed in this study are described in the SI sections Text S1. Details pertaining to characterizations are shown in Text S2–S4.

2.2 Catalyst preparation

2.2.1 ZIF-8, ZIF-ZnO and ZnO@CNT preparation. Dissolve 0.73 g of zinc nitrate hexahydrate in a beaker with 50 mL of methanol solution, and similarly dissolve 0.82 g of 2-methylimidazole in another beaker containing 50 mL of methanol solution. Subsequently, the methanol solution dissolved in zinc nitrate hexahydrate was quickly poured into the methanol solution containing 2-methylimidazole, stirred immediately, and the mixed solution was stirred thoroughly at a speed of 800 rpm for 24 hours. After stirring, let the mixed solution stand for 24 hours. After the solution is layered and precipitated, the product is centrifuged, washed with methanol at least three times, and then dried into a powder in a vacuum. The resulting product is denoted as ZIF-8. Subsequently, the prepared powder is heated to 800 °C in a tube furnace under the protection of nitrogen at a rate of 5 °C min^{-1} and calcined for 6 hours. The resulting product is denoted as ZIF-ZnO. Following this procedure, the addition of carbon nanotubes in the initial step yielded the final composite, which was named ZnO@CNT (Fig. 1).

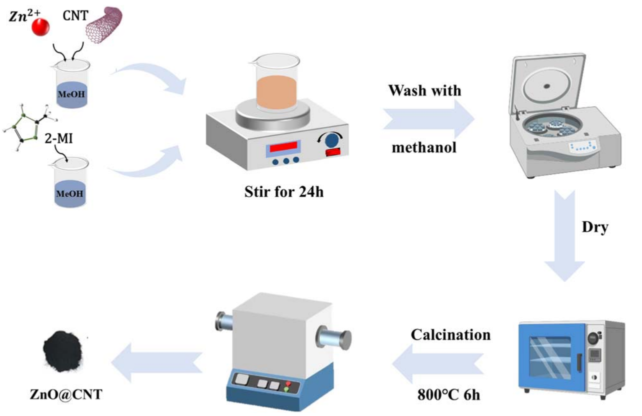

Fig. 1 The preparation process of ZnO@CNT.

2.3 Catalyst performance

Under standard conditions at 25 °C, all reactions were performed by employing magnetic stirring to disperse the catalyst (10 mg) and PDS (50 mg) in a 50 mL SMX solution (20 mg L^{-1}) within a 100 mL reactor. To examine the role of different anions in the degradation process, common anions such as nitrate (NO_3^-), bicarbonate (HCO_3^-), humic acid (HA) and chloride (Cl^-) were added to the experimental system to simulate the actual wastewater environment. At a preset time node, 1.5 mL of the reaction solution was taken from the reaction mixture, filtered through a 0.22 μm polytetrafluoroethylene (PTFE) membrane, and collected in a plastic centrifuge tube preloaded with 200 μL (12 g L^{-1}) of sodium sulfite ($Na_2S_2O_3$) stop solution to immediately terminate the oxidation reaction. All samples were finally analyzed by high-performance liquid chromatography (LC-20AT) for residual concentrations of SMX.

3 Results and discussion

3.1 Material characterization

The SEM and TEM micrographs as well as the corresponding elemental maps of the ZnO@CNT composite are presented in Fig. 2. The SEM images in Fig. 2(a and b) reveal partial

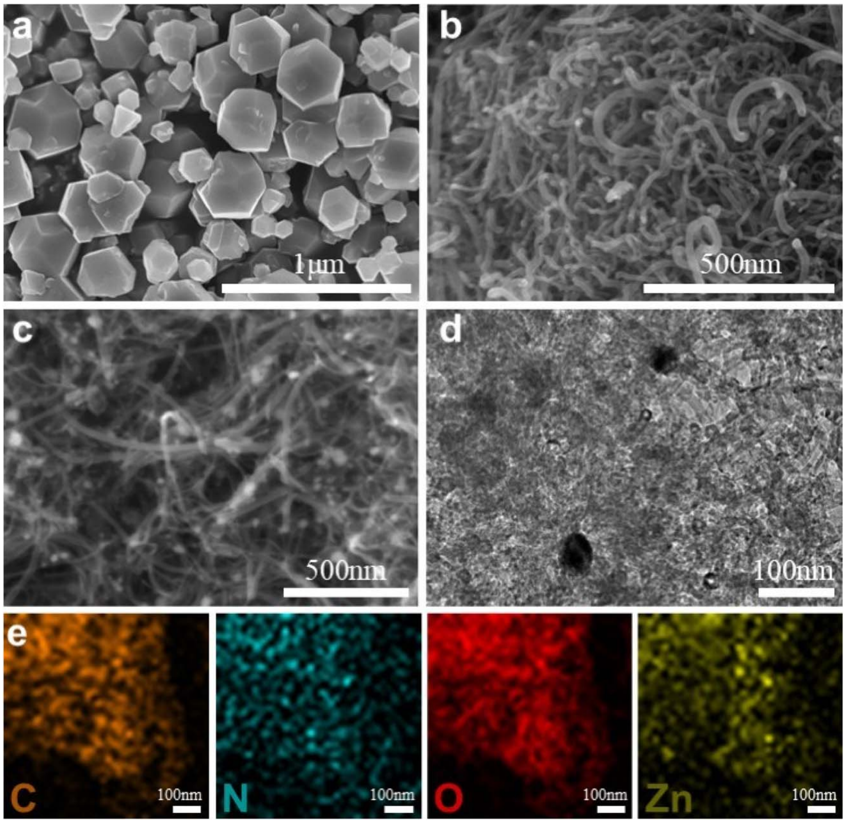

Fig. 2 SEM images of ZIF-8 (a), CNTs (b) and ZnO@CNT (c); TEM images of ZnO@CNT (d); EDS mapping images (e).

agglomeration of ZIF-8-derived particles, limiting the full utilization of the material's specific surface area. The carbon nanotubes retain an intact tubular structure with a random stacking arrangement, while ZnO nanoparticles (black speckles) are homogeneously distributed across the surfaces of the carbon nanotubes as shown in Fig. 2(c and d). This unique structural feature indicates that ZnO particles are efficiently loaded and dispersed both inside and outside the catalyst skeleton. This not only effectively inhibits the dissolution of zinc ions, but also significantly reduces particle aggregation, thereby improving the catalyst's catalytic performance, cycling stability, and reusability. EDS surface scanning analysis (Fig. 2(e)) confirmed the uniform distribution of carbon, oxygen and zinc in the composites, thus providing definitive evidence for successful material synthesis. In terms of mass percentage, the contents of C, N, O and Zn were 77.73%, 0.81%, 5.46% and 16.00% respectively. These findings correlated well with the morphological characterization data, thus confirming the compositional and structural integrity of the ZnO@CNT composites.

A comparative analysis of the XRD spectra of ZIF-8, CNTs and ZnO@CNT composites is shown in Fig. 3(a). The ZnO@CNT XRD spectra show significant characteristic diffraction peaks at $2\theta = 31.69°$, $34.38°$, $36.18°$, $47.45°$ and $56.46°$, which correspond to the (100), (002), (101), (102) and (110) crystal faces of hexagonal fibrillar zincite structure ZnO (ICDD #01-079-0207).[30] Notably, both the characteristic diffraction peaks of CNTs (26°) and ZnO are present in the XRD spectra. The crystallographic data thus attest to the successful integration of ZnO with the CNT support, confirming the formation of the ZnO@CNT

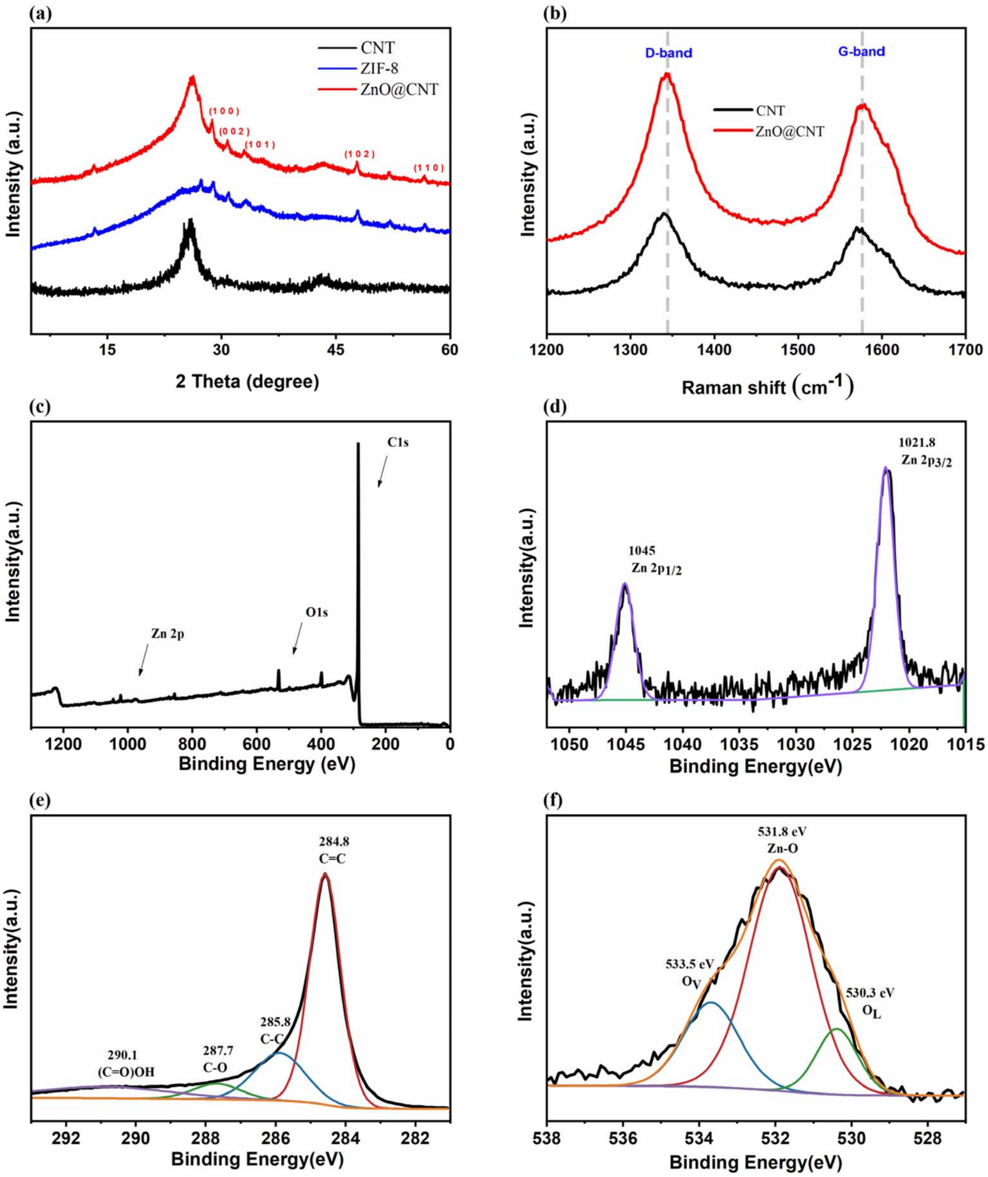

Fig. 3 XRD patterns of ZIF-8, CNTs and ZnO@CNT (a). Raman spectra of CNTs and ZnO@CNT (b). XPS spectra of ZnO@CNT: full spectra (c); Zn 2p (d); C 1s (e); O 1s (f).

composite. The sharpness of the diffraction peak shapes indicates that the prepared ZnO has a high degree of crystallinity, and the precise matching of the characteristic peak positions excludes the presence of other zinc compounds.

The surface defect states of the catalysts were investigated by Raman spectroscopy (Fig. 3(b)). The spectra clearly showed the characteristic D (1331 cm^{-1}) and G (1593 cm^{-1}) bands in both the CNT and ZnO@CNT samples.[31] The D band signifies structural disorder and the G band corresponds to sp^2 hybridized carbon. Consequently, the intensity ratio of D and G bands (I_D/I_G) serves as a metric for quantifying the defect density within the material.[32] Fig. 3(b) reveals an increase in the I_D/I_G value from 0.77 (CNT) to 0.86 (ZnO@CNT), implying that the integration of ZnO created more defective structures. This confirms that ZnO integration introduced additional defects, which function as active sites to enhance reactant adsorption and activation, thereby promoting the catalytic process.

The XPS characterization results of ZnO@CNT are presented in Fig. 3(c). The spectrum shows four obvious sub-peaks, which correspond to the following bonds: C=C (284.8 eV), C–C (285.8 eV), C–O (287.7 eV), and COOH (290.1 eV) bonds.[33,34] This indicates that carbon atoms in ZnO@CNT composite materials exist in various forms and form different chemical bonds with other elements. For the O 1s peak, as shown in Fig. 3(f), two obvious peaks were observed at 533.5 eV and 530.3 eV, corresponding to oxygen vacancies (OV) and lattice oxygen (OL), respectively.[35] Additionally, the peak at 531.8 eV is consistent with the Zn–O bond, further confirming the presence of Zn oxide. Fig. 3(d) shows that the Zn 2p spectrum exhibits two peaks at 1021.8 eV and 1045 eV, corresponding to the Zn $2p_{3/2}$ and Zn $2p_{1/2}$ binding energies of the Zn–O bond respectively, providing further confirmation of Zn oxide.[36,37]

3.2 Catalytic performance

For a comprehensive performance evaluation of CNTs, ZIF-8, ZIF-ZnO and ZnO@CNT toward PDS activation, SMX was employed as the model pollutant. To establish the optimal formulation, a series of ZnO@CNT catalysts with varying ZnO loadings (5%, 10%, 15%, 20%, and 25%) were synthesized and evaluated for SMX degradation under identical conditions (SI, Fig. S5). Among these, ZnO@CNT-15 (15% loading) exhibited the highest degradation efficiency (90.3% within 30 min) and was therefore selected as the optimal catalyst for subsequent investigations. The degradation performance of each catalyst was subsequently assessed and compared. As illustrated in Fig. 4(a), the control experiments employing PDS alone, CNTs alone, or ZnO@CNT alone achieved the lowest SMX removal rates of merely 3.72%, 11.43%, and 12.71%, respectively. This indicates that neither ZnO@CNT nor CNTs exhibits satisfactory catalytic performance when used individually. After 30 minutes of reaction in the presence of PDS, the ZIF-8/PDS and CNT/PDS systems reached SMX removal rates of only 19.32% and 46.81%, respectively, demonstrating limited catalytic activity of both ZIF-8 and CNTs in activating PDS for SMX degradation. To further decouple the intrinsic catalytic activity of ZnO from the synergistic effects arising from the ZnO–CNT interface, we evaluated the performance of ZIF-8-derived pure ZnO (ZIF-ZnO) as an additional control under identical conditions. The ZIF-

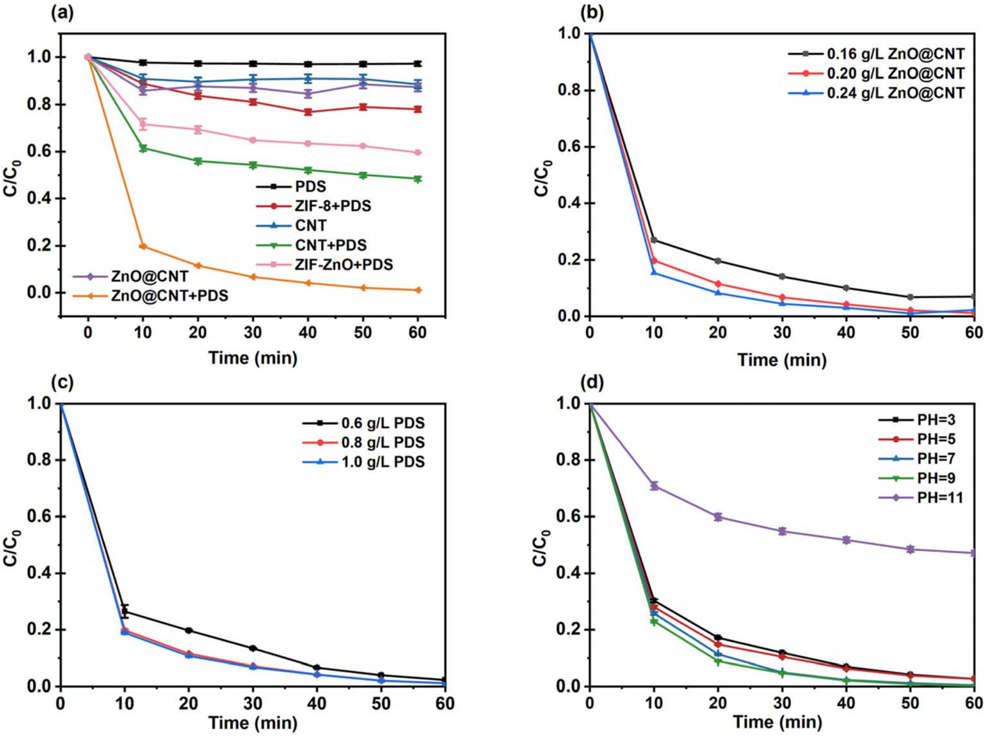

Fig. 4 Different SMX degradation reaction systems (a) experimental: 0.8 g per L PDS, 20 mg per L SMX, 0.2 g per L ZnO@CNT, pH 9, 25 °C; different ZnO@CNT dose (b); different PDS doses (c); different pH values (d).

ZnO/PDS system achieved only 35.0% SMX removal within 30 minutes and 40.5% removal within 60 minutes, confirming that pure ZnO also possesses limited intrinsic catalytic activity for PDS activation. Notably, the degradation efficiency of ZIF-ZnO/PDS (40.5% at 60 min) is even lower than that of CNT/PDS (46.81% at 30 min), indicating that neither component alone is sufficient for efficient SMX degradation. In contrast, under identical reaction conditions (30 minutes), the ZnO@CNT/PDS system achieved a markedly higher SMX removal efficiency of 93.56%, significantly surpassing those of the ZIF-8/PDS, ZIF-ZnO/PDS, and CNT/PDS systems. This dramatic enhancement, with an enhancement factor of approximately 2.5 compared to the sum of individual activities, provides compelling evidence that the superior performance of ZnO@CNT arises from the synergistic effect at the ZnO–CNT interface, which facilitates electron transfer and promotes PDS activation. The apparent rate constant of the ZnO@CNT/PDS system was 0.089 min^{-1}, representing a 13-fold and 4.5-fold increase over the ZIF-8/PDS (0.00695 min^{-1}) and CNT/PDS (0.021 min^{-1}) systems, respectively. This significant difference in k_{obs} values highlights the superior catalytic efficiency of the ZnO@CNT composite. The ZnO@CNT/PDS system showed superior performance compared to other catalysts in the literature (Table 1), reaching 93.56% efficiency and a rate constant of 0.089 min^{-1}, owing predominantly to the involvement of $^1O_2$.

The catalytic performance of ZnO@CNT was further evaluated by varying key parameters, including catalyst and PDS concentrations, as well as solution pH. Fig. 4(b) illustrates the effect of catalyst dosage on SMX removal. As the ZnO@CNT concentration from 0.16 to 0.20 g L^{-1} enhanced SMX degradation, with efficiency climbing from 85.82% to 93.23% over 30 minutes. This improvement is attributed to the increased availability of active sites at higher catalyst doses, which promotes PDS activation and accelerates the reaction kinetics. Notably, no simple linear correlation exists between catalyst dosage and degradation efficiency. This is exemplified by the observation that while a higher catalyst dosage (0.20 g L^{-1}) afforded faster degradation compared to a lower one (0.16 g L^{-1}), the increasing trend was not significant. When the dosage was further increased to 0.24 g L^{-1}, the improvement in SMX degradation efficiency was only marginal, reaching 93.53%. This plateau likely occurs because, beyond an optimal catalyst loading, the fixed concentration of PDS becomes the limiting factor, and the excess active sites cannot be fully utilized to further accelerate the reaction. The high efficiency already achieved with a moderate ZnO@CNT dosage (0.20 g L^{-1}) highlights the significance of the material's design. Future research should focus on optimizing catalyst–oxidant combinations to balance cost and performance.

A key parameter governing the degradation efficacy was the PDS dosage. As shown in Fig. 4(c), elevating the PDS concentration from 0.6 g L^{-1} to 0.8 g L^{-1} markedly boosted the SMX degradation from 86.59% to 93.23% in 30 minutes. Under conditions where the catalyst amount (total number of active sites) is fixed and the PDS concentration remains below saturation, increasing the PDS concentration significantly enhances its adsorption concentration on the catalyst surface and increases the collision frequency at the active sites. This directly drives the activation of more PDS molecules, thereby amplifying reactive species production. The system, however, exhibits saturation behavior, as increasing the PDS dose to 1.0 g L^{-1} provided only a minimal efficiency gain to 93.82%, underscoring the constrained benefit of excessive oxidant addition. While high PDS concentrations provide abundant reactant molecules, the limited availability of catalytic sites becomes saturated, thereby hindering further activation. To balance economic efficiency with the goal of definitive SMX removal, a combination of 0.2 g per L ZnO@CNT and 0.8 g per L PDS was identified as the optimum condition for all subsequent experiments.

Solution pH significantly influenced SMX degradation efficiency. As depicted in Fig. 4(d), the 30 minute SMX removal rate improved from 88.11% at pH 3.0 to 92.47% at pH 7.0, and reached 93.56% under alkaline conditions (pH 9.0). However, at a pH of 11, degradation efficiency was inhibited. Zeta potential measurements confirmed that the point of zero charge (PZC) of ZnO@CNT is 8.6 (SI: Fig. S6). Below the PZC (pH 3.0–8.6), the positively charged catalyst surface facilitates interaction with SMX. The efficiency increased progressively from pH 3.0 to 7.0, attributed to enhanced electrostatic attraction with anionic SMX ($pK_{a_2} = 5.7$).[43] Interestingly, the peak efficiency was achieved at pH 9.0, where the catalyst surface becomes negatively charged (pH > PZC). This apparent paradox is explained by the dominance of the non-radical pathway under weakly alkaline conditions: abundant $^1O_2$ generated at pH 9.0 can still reach SMX despite mild electrostatic repulsion. However, at pH 11, the strong negative charge creates intense electrostatic repulsion, physically separating SMX from the catalyst surface.[44] Even if $^1O_2$ generation is enhanced *via* radical conversion pathways, the short-lived $^1O_2$ cannot effectively diffuse across this repulsion barrier, leading to a sharp decline in degradation efficiency. Under highly acidic conditions (pH = 3.0), an

Table 1 Comparative analysis of SMX degradation efficiency, rate constants and ROS pathways with varied catalysts/oxidants

Samples	Catalyst dosage	Oxidant dosage	SMX conc.	Reaction time	Degradation efficiency (%)	Rate constant (min^{-1})	Ref.
ZnO@CNT	200 mg L^{-1}	PDS (0.8 g L^{-1})	20 mg L^{-1}	60 min	93.56	0.089	This work
2.0-NMC	200 mg L^{-1}	PS (2 g L^{-1})	20 mg L^{-1}	60 min	81.4	0.025	38
NMC-50	50 mg L^{-1}	PMS (0.65 mM)	15 mg L^{-1}	60 min	87.37	0.045	39
BC/Fe(III)	500 mg L^{-1}	PDS (0.5 g L^{-1})	10 mg L^{-1}	90 min	80.5	0.0188	40
CNT	100 mg L^{-1}	PDS (500 μM)	2 mg L^{-1}	60 min	68.8	0.0255	41
MG0.2	50 mg L^{-1}	PMS (0.5 mM)	5 mg L^{-1}	120 min	86	—	42

abundance of H^+ scavenges both $SO_4^{\bullet -}$ and $^{\bullet}OH$ radicals, contributing to the lower removal rate.

3.3 Mechanism

3.3.1 Identification of active substances during SMX degradation. To identify the reactive species responsible for SMX degradation in the ZnO@CNT/PDS system, EPR spectroscopy and radical quenching tests were employed in tandem. As illustrated in Fig. 5(a), the key radical species were probed using *tert*-butanol (TBA), methanol (MA), *p*-benzoquinone (*p*-BQ), and L-histidine as quenching agents.[45,46] Among them, TBA was assigned to capture $^{\bullet}OH$, and MA to eliminate both $SO_4^{\bullet -}$ and $^{\bullet}OH$. In the presence of sufficient TBA and MA, the SMX removal within 30 minutes experienced a slight decrease to 92.35% and 91.55%, respectively, from an original value of 93.75%. Furthermore, when the $O_2^{\bullet -}$ scavenger *p*-BQ was introduced into the system, a significant reduction in SMX removal efficiency was observed. Upon introduction of the $^1O_2$ scavenger L-histidine, the SMX removal rate plummeted to 27.43%. In summary, $^1O_2$ serves as the primary driving force for SMX degradation, with $O_2^{\bullet -}$, $SO_4^{\bullet -}$, and $^{\bullet}OH$ radicals providing secondary contributions ($^1O_2 \gg O_2^{\bullet -} > SO_4^{\bullet -} > {}^{\bullet}OH$).

The identification of active species in the ZnO@CNT/PDS system was unequivocally confirmed by EPR spectroscopy (Fig. 5(b and c)). The absence of characteristic signals in control experiments with PDS and DMPO thus confirms that PDS self-decomposition is negligible. However, after adding ZnO@CNT/PDS, a distinct DMPO–$O_2^{\bullet -}$ signal was detected. The presence of this signal highlights the contribution of $O_2^{\bullet -}$ radicals in the activation of PDS, which aligns with the results from the radical quenching experiments.[47] Additionally, in the ZnO@CNT/PDS system, TEMP (a trapping agent for $^1O_2$) was used, and a characteristic triplet signal (1 : 1 : 1) was observed. This observation confirms the presence of a considerable amount of $^1O_2$ during the activation of PDS.[48] This finding corroborates the previous experimental results, further demonstrating the significant role of non-radical active species in the degradation of SMX. In summary, EPR analysis and quenching tests confirmed the coexistence of both free radical and non-radical pathways in the ZnO@CNT/PDS system. Among them, $^1O_2$ was identified as the predominant reactive species.

Electron transfer represents a pivotal non-radical pathway for PDS activation. In the ZnO@CNT/PDS system, this pathway was investigated *via* an integrated approach of chronoamperometry and DFT. The *IT* response in Fig. 5(d) exhibited marked shifts upon the sequential introduction of PDS and SMX, which validates the direct electron transfer from the oxidant to the pollutant and confirms its critical function.[49]

3.3.2 Catalytic mechanism. To comprehensively evaluate the electronic transport properties of ZIF-8, CNTs, and ZnO@CNT, electrochemical characterization coupled with theoretical computational analysis was conducted in this study. Fig. S7(a) demonstrates that the impedance spectrum semicircle diameter of ZnO@CNT is markedly smaller than that of ZIF-8 and CNTs, indicating lower electrical resistance and superior electronic transport capability.[50] Further DFT calculations revealed the electronic structural characteristics of the

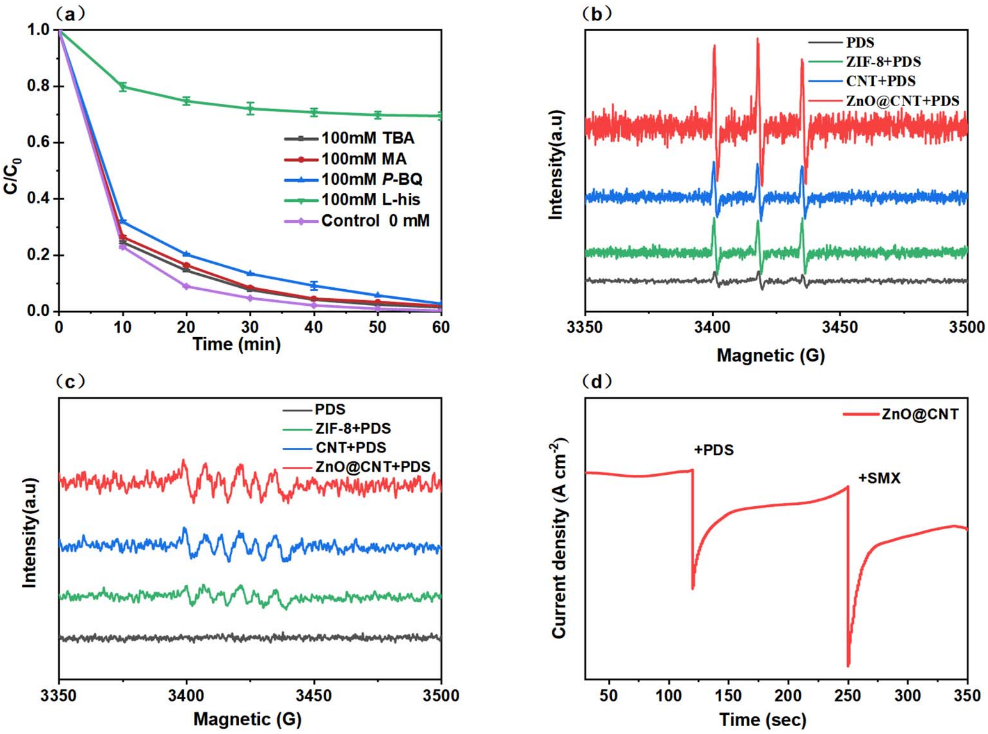

Fig. 5 Quenching effects on SMX degradation (a); EPR spectra with TEMP (for $^1O_2$) and DMPO (for $O_2^{\bullet -}$), respectively (b and c); *IT* curve of ZnO@CNT/PDS (d). Reaction conditions: 20 mg per L SMX, 0.2 g per L ZnO@CNT, 0.8 g per L PDS, pH 9, 25 °C.

materials (Fig. S7(b)). Furthermore, the Fermi level of the material was calculated, which is a pivotal parameter for measuring the material's capacity to gain or lose electrons.[51] ZnO has been successfully loaded onto the inner walls of carbon nanotubes, with Fermi levels reaching 2.09 eV for ZnO@CNT, surpassing those of ZIF-8 (1.55 eV) and CNTs (1.99 eV). This outcome demonstrates that ZnO@CNT exhibits enhanced charge acquisition and delivery capabilities, significantly boosting electron transfer efficiency during the catalytic process.[52]

A critical factor in accelerated electron transfer is the tailored electronic structure, driven by the ZnO–CNT interaction and the ensuing p-orbital hybridization with carbon. In the ZnO@CNT hybridized configuration, the formation of bonding and anti-bonding orbitals is observed, and the bonding orbital is chiefly occupied by electrons originating from the ZnO HOMO. Differences in the electronic properties among CNTs, ZnO, and ZnO@CNT provide deeper insight into the interfacial interaction-induced electronic structure modulation. The HOMO of pristine CNTs features carbon p-orbital electrons, contrasting with ZnO, where the HOMO consists of oxygen orbitals with substantial zinc p-orbital character (Fig. S7(c and d)). Composite formation elevates the HOMO energy of ZnO and intensifies its orbital charge localization—a modification that positively influences catalysis. The disruption of strong ionic electron localization by incorporating ZnO into CNTs yields an extended valence band and greater carrier mobility.[53] Consequently, ZnO@CNT displays superior electron activity, which enhances its catalytic reactivity. The potential adsorption model of PDS molecules on ZnO@CNT is shown in Fig. S8. The adsorption energy for CNTs is −0.6479 eV, while for ZnO@CNT it is −1.152 eV. The higher ΔE_{ads} value indicates a stronger binding affinity of ZnO@CNT toward PDS molecules, facilitating PDS activation and the formation of non-radical species ($^1O_2$) within the catalyst cavity. Ultimately, zinc doping is a viable tactic for advancing the electron transfer performance of CNTs by enabling more effective electronic structure regulation to optimize catalytic activity.

Collectively, these findings demonstrate that SMX degradation is primarily dominated by the non-radical pathway mediated by singlet oxygen ($^1O_2$), while concurrently influenced by the synergistic contribution of radical species ($^{\bullet}OH$, $SO_4^{\bullet-}$, and $O_2^{\bullet-}$). The proposed catalytic mechanism is illustrated in Fig. S9. Initially, at the ZnO@CNT heterojunction interface, the Zn^{2+} sites on the ZnO surface synergize with CNTs to activate PDS *via* interfacial electron transfer, leading to the cleavage of the O–O bond and the generation of initial radicals (eqn (A1)). The subsequent conversion of these primary radicals leads to the formation of $O_2^{\bullet-}$ (eqn (A2)–(A5)), which is a key precursor for $^1O_2$ generation (eqn (A6) and (A7)).

$$S_2O_8^{2-} + e^- \rightarrow SO_4^{\bullet-} + SO_4^{2-} \tag{A1}$$

$$SO_4^{\bullet-} + H_2O \rightarrow {}^{\bullet}OH + SO_4^{2-} + H^+ \tag{A2}$$

$$^{\bullet}OH + {}^{\bullet}OH \rightarrow H_2O_2 \tag{A3}$$

$$^{\bullet}OH + H_2O_2 \rightarrow HO_2^{\bullet} + H_2O \tag{A4}$$

$$HO_2^{\bullet} \rightarrow H^+ + O_2^{\bullet-} \tag{A5}$$

$$O_2^{\bullet-} + HO_2^{\bullet} \rightarrow {}^1O_2 + HO_2^- \tag{A6}$$

$$2O_2^{\bullet-} + 2H^+ \rightarrow {}^1O_2 + H_2O_2 \tag{A7}$$

$$\text{Defective carbon} + \text{PDS} \rightarrow {}^1O_2 + 2SO_4^{2-} \tag{A8}$$

$$\text{SMX} + \left(SO_4^{\bullet-}/{}^{\bullet}OH/O_2^{\bullet-}/{}^1O_2\right) \xrightarrow{e^-} \cdots \rightarrow CO_2 + H_2O \tag{A9}$$

Defects in carbon-based nanomaterials are instrumental in generating singlet oxygen ($^1O_2$) by acting as active sites for this reaction.[18] This view is supported by the intensified characteristic XRD peaks of CNTs after the reaction (Fig. 6(b)), underscoring their crucial function. Specifically, CNT surface defects are proposed as catalytic centers for peroxydisulfate activation (eqn (A8)), which subsequently boosts singlet oxygen yield and robustly facilitates pollutant removal—a rationale widely adopted in CNT/PDS research. Concurrently, direct electron transfer *via* CNTs constitutes another essential component in the ZnO@CNT/PDS system. Evidence from quenching experiments affirms its key function in the catalytic mechanism,[54] accelerating the reaction rate (eqn (A9)).

3.4 Stability and general applicability of catalysts

In the practical application of catalysts, stability and reusability are critical factors to consider. To comprehensively evaluate the reusability of the ZnO@CNT catalyst, we conducted five consecutive cycles of experiments under identical reaction conditions (see Fig. 6(a)). The results show that after five cycles, ZnO@CNT maintained a high degradation efficiency (80.3%), demonstrating its excellent stability and reusability. It was found that Zn^{2+} inevitably leaches from the material, with a leaching concentration of 0.32 mg L^{-1}, which is below the limit specified by China's drinking water hygiene standard (CB5749-2022) of 1 mg L^{-1}. The slight leaching of zinc ions leads to the deactivation of a portion of the active sites, which reduces the catalytic activity of the material. However, the structure of CNTs in the catalyst still remains stable.

The catalyst's performance was further verified by employing CIP, DF, and BPA as representative substrates to evaluate its efficacy across diverse antibiotics. As shown in Fig. S10, removal efficiencies exceeding 87% were achieved for all tested contaminants within 60 minutes, demonstrating its excellent applicability for eliminating diverse antibiotics.

Additionally, the characteristic diffraction peak of the carbon nanotubes at 26.1° showed a slight increase in intensity after reuse, indicating an improvement in the crystallinity of the material. This is likely due to the selective etching of unstable amorphous carbon and some structural defects on the surface of the carbon nanotubes by reactive oxygen species in the highly oxidative reaction environment, leaving behind a more stable graphitic skeleton. However, such surface etching and structural reorganization are key reasons for the decline in catalytic

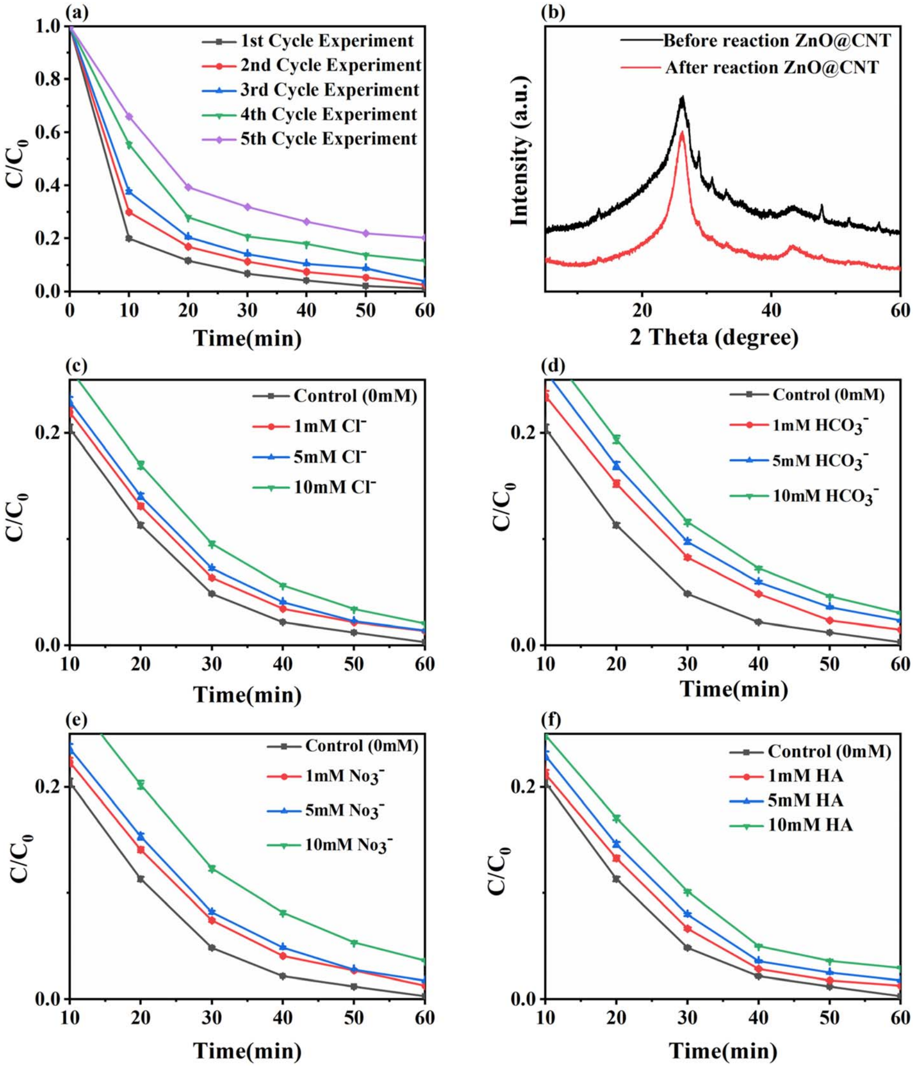

Fig. 6 ZnO@CNT degradation cycle experiment of SMX in the PDS system (a); ZnO@CNT XRD patterns before and after the reaction (b); degradation of ZnO@CNT/PDS under Cl^- conditions (c); degradation of ZnO@CNT/PDS under HCO_3^-conditions (d); degradation of ZnO@CNT/PDS under NO_3^- conditions (e) and degradation of ZnO@CNT/PDS under HA conditions (f).

activity.[18] The catalytically active sites in the carbon nanotube/PDS system are typically associated with edge sites, heteroatom-doped sites, or specific structural defects. In this experiment, although the reaction-induced surface etching slightly enhanced the overall crystallinity, it also destroyed these critical active defect structures, thereby weakening the catalyst's ability to activate PDS. Furthermore, the strong adsorption and accumulation of organic intermediates generated during the reaction on the surface of the carbon nanotubes can physically block the remaining active sites, further hindering the contact between PDS and the catalyst. Thus, the decrease in catalyst activity during repeated use is closely related to both the structural changes in the carbon nanotubes and the adsorption of intermediates.

Inorganic anions (such as NO_3^-, HCO_3^- and Cl^-) and organic substances like humic acid (HA) in wastewater often influence the decomposition of PDS as shown in Fig. 6(c–f). Specifically, the addition of chloride (Cl^-) at different concentrations slightly inhibited SMX degradation: when Cl^- was added at concentrations of 1, 5, and 10 mM, the SMX removal rate within 30 minutes decreased from 95.1% to 93.7%, 92.8%, and 90.5%, respectively. This decline results from dual inhibitory mechanisms: Cl^- consumes $SO_4^{\bullet -}$ to yield lower-potential radicals (eqn (A10)–(A13)), while HCO_3^- significantly hinders degradation by scavenging $SO_4^{\bullet -}$ and $^{\bullet}OH$ to form less reactive species (eqn (A14) and (A15)), respectively.[55] Similarly, NO_3^- also affected SMX degradation, but its inhibitory effect was relatively weaker (eqn (A16)). Furthermore, as the concentration of HA increased, the SMX removal rate within 30 minutes decreased from 95.1% to 89.9%. The reasons for this may include: firstly, oxygen-containing functional groups (such as hydroxyl) in HA can adsorb onto the catalyst surface, compromising its ability to interact with and activate PDS;[28,56] secondly, humic acid may shield active sites through strong π–π stacking effects, potentially preventing interactions between the catalyst surface and both PDS and SMX molecules.[57] Overall, these observations indicate that various anions and humic acids only slightly inhibit the degradation efficiency, highlighting the good stability of this catalyst in practical applications.

$$SO_4^{\bullet -} + Cl^- \rightarrow SO_4^{2-} + Cl^{\bullet} \quad (A10)$$

$$Cl^{\bullet} + H_2O \rightarrow ClOH^{\bullet -} + H^+ \quad (A11)$$

$$ClOH^{\bullet -} + Cl^- \rightarrow Cl_2^- + OH^- \quad (A12)$$

$$Cl^{\bullet} + Cl^{\bullet} \rightarrow Cl_2 \quad (A13)$$

$$SO_4^{\bullet -} + HCO_3^- \rightarrow CO_3^- + SO_4^{2-} + H^+ \quad (A14)$$

$$^{\bullet}OH + HCO_3^- \rightarrow CO_3^- + H_2O \quad (A15)$$

$$SO_4^{\bullet -} + NO_3^- \rightarrow CO_3^{\bullet -} + H_2O \quad (A16)$$

3.5 Degradation pathway of SMX

To elucidate the degradation mechanism of SMX (Fig. 7(a)) at the molecular level, this study employed comprehensive density functional theory (DFT) calculations. A systematic analysis combining frontier molecular orbital (HOMO/LUMO) distributions, natural population analysis (NPA) charge, and Fukui indices (Fig. 7(b, c) and Table 2) enabled the precise identification of key reactive sites in the SMX molecule. The HOMO distribution (Fig. 7(b)) demonstrates that atoms on the isoxazole ring, including 9O, 10O, 7N, and 17N, serve as the primary electron-donating centers.[58,59] This observation correlates well with their highly negative NPA charges (all below −0.78), collectively indicating the high susceptibility of these sites to electrophilic attack. Meanwhile, the Fukui index (f^0) values in Table 2 reveal another category of highly active sites, namely 13C, 17N, 15C, and 16C (all with f^0 values greater than

Table 2 The Hirshfeld charge and Fukui function of every atom in SMX

No.	Atom	NPA	f^+	f^-	f^0
1	C	−0.65568	0.0069	0.0100	0.0084
2	C	0.34579	0.0153	0.0262	0.0207
3	C	−0.3862	0.0016	0.0062	0.0039
4	C	0.29089	-0.002	0.0053	0.0017
5	N	−0.17397	0.026	0.0251	0.0255
6	O	−0.28935	0.0245	0.0262	0.0254
7	N	−0.83838	0.0463	0.0159	0.0311
8	S	2.31648	0.015	0.0182	0.0166
9	O	−0.93226	0.0398	0.0312	0.0355
10	O	−0.93877	0.0387	0.0305	0.0346
11	C	−0.40937	0.0878	0.0262	0.057
12	C	−0.14946	0.0354	0.0708	0.0531
13	C	−0.26509	0.0717	0.1025	0.0871
14	C	0.18892	0.0571	0.0393	0.0482
15	C	−0.26314	0.0679	0.0883	0.0781
16	C	−0.15153	0.0379	0.1047	0.0713
17	N	−0.78593	0.1432	0.029	0.0861
18	H	0.23194	0.008	0.0103	0.0092
19	H	0.23614	0.0072	0.0125	0.0099
20	H	0.23835	0.0138	0.0175	0.0156
21	H	0.26374	0.0069	0.0089	0.0079
22	H	0.42448	0.016	0.0222	0.0191
23	H	0.24346	0.0274	0.0379	0.0326
24	H	0.21685	0.036	0.0612	0.0486
25	H	0.21783	0.0357	0.0522	0.044
26	H	0.24405	0.0295	0.0577	0.0436
27	H	0.38994	0.0529	0.033	0.043
28	H	0.39027	0.0533	0.0293	0.0413

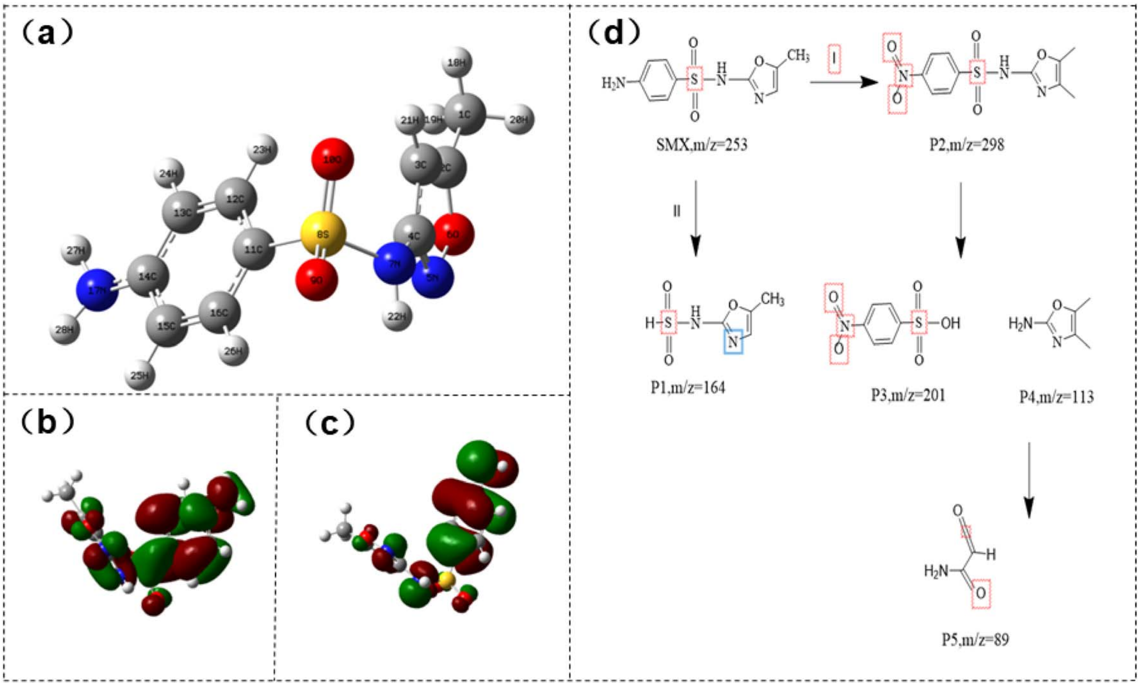

Fig. 7 SMX structural model (a), HOMO isodensity surface of SMX (b), LUMO isodensity surface of SMX (c), and degradation pathway of SMX (d).

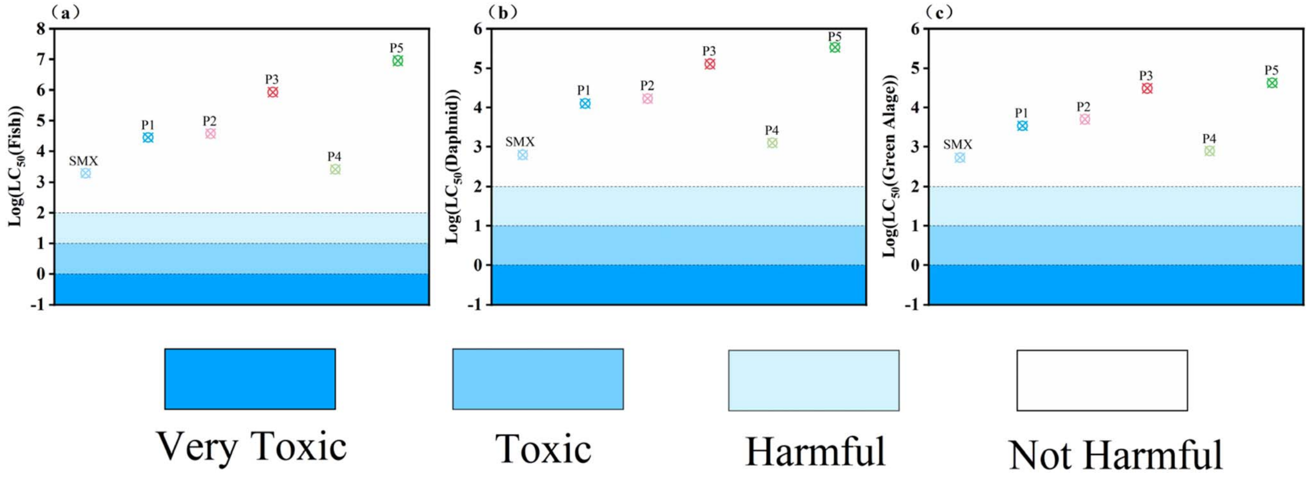

Fig. 8 ECOSAR toxicity data of fish (a), daphnid (b), and green algae (c).

0.071), which exhibit significant sensitivity to radical attack. These highly reactive sites are predominantly concentrated on the benzene and isoxazole ring structures, providing clear theoretical targets for subsequent degradation pathway speculation.

Based on the identified degradation products and pathways shown in Fig. 7(d), the degradation mechanism of SMX in the ZnO@CNT/PDS system can be elucidated as follows. The primary reactive sites, as determined by Fukui index analysis, are predominantly located on the benzene and isoxazole rings rather than the amino groups. These sites, characterized by high electron density and Fukui indices, are susceptible to attacks by various radical species (*e.g.*, $^{\bullet}OH$, $SO_4^{\bullet-}$, and $O_2^{\bullet-}$) and non-radical species (*e.g.*, $^1O_2$), initiating a series of chemical transformations. The degradation proceeds through multiple pathways: (1) hydroxylation and ring cleavage of the benzene ring, generating intermediate P1 ($m/z = 164$, $[m + H]^+$);[60] (2) oxidation of the isoxazole ring, leading to the formation of P2 ($m/z = 224$, $[m + H]^+$); (3) further cleavage and rearrangement producing P3 ($m/z = 201$, $[m + H]^+$) and P4 ($m/z = 113$, $[m + H]^+$);[61] and (4) eventual conversion to smaller organic acids such as P5 ($m/z = 89$, $[m + H]^+$),[62] culminating in complete mineralization to CO_2 and H_2O. The TOC removal efficiency of 56.36% (Fig. S11) confirms the significant mineralization capability of the ZnO@CNT/PDS system. This outcome confirms the validity of the proposed degradation mechanism while highlighting the system's promise for practical antibiotic wastewater treatment.

3.6 Toxicity assessment of SMX degradation products

The acute aquatic toxicity of SMX and its degradation intermediates was evaluated using ECOSAR-predicted data (Fig. 8), with a toxicity classification threshold of $\log_{10} > 2.0$ indicating non-toxic substances. The pristine SMX demonstrated $\log_{10}$ values exceeding the 2.0 threshold for all three aquatic test species, confirming its classification as non-toxic. Following treatment in the ZnO@CNT/PDS system, all degradation products exhibited significantly increased $\log_{10}$ values, demonstrating effective toxicity reduction. Particularly noteworthy were the markedly elevated values for P2, P3, and P5, indicating substantially diminished environmental risk. Although P4 exhibited relatively higher toxicity among the degradation products, particularly toward green algae where values approached the toxicity threshold, all measured values remained above the 2.0 criterion and showed marked improvement compared to pristine SMX. These quantitative findings validate that the degradation process successfully achieves effective detoxification, with the deeply oxidized products P3 and P5 displaying exceptional environmental safety characteristics. This investigation provides crucial evidence for evaluating the ecological safety of this advanced oxidation process and demonstrates its potential for mitigating environmental risks associated with antibiotic contaminants.

4 Conclusion

(1) The ZnO@CNT catalyst, synthesized *via* one-pot pyrolysis, leverages the synergy between ZnO and CNTs to activate PDS exceptionally well, achieving a k_{obs} of 0.089 min^{-1} that surpasses its individual components. This underscores the role of ZnO in enhancing electron transfer and ROS generation. The composite design overcomes the limitations of metal-based catalysts and carbon materials, while maintaining high effectiveness across a broad pH range (3–9).

(2) The system operates *via* a singlet oxygen ($^1O_2$)-dominated non-radical pathway, which provides superior selectivity, resistance to environmental interference, and broad-spectrum efficacy against various antibiotics.

(3) DFT calculations and electrochemical analyses further elucidate how ZnO doping optimizes the electronic structure to favor the PDS → $^1O_2$ conversion. Practical applicability is highlighted by the catalyst's stability (80.3% efficiency retention after 5 cycles) and environmental compatibility, as confirmed by ECOSAR assessment of reduced intermediate toxicity. These attributes position ZnO@CNT as a robust and versatile solution for real-world water remediation.

Author contributions

Qian Zhou: conceptualization, methodology, visualization, writing-original draft. Qingsong Liu: writing-review & editing. Chenglin Li: formal analysis. Liu Yang: data curation. Yu Xue: resources. Shengqiong Fang: conceptualization, supervision, project administration, funding acquisition. Weiguang Lan: conceptualization, supervision, project administration.

Conflicts of interest

There are no conflicts to declare.

Data availability

The datasets supporting this article have been uploaded as part of the supplementary information (SI). Supplementary information: experimental materials (S1), experimental parameters (S2), theoretical calculation details (S3 and S4), degradation efficiency of SMX by ZnO@CNT with different loadings (Fig. S5), zeta potential of ZnO@CNT under different pH conditions (Fig. S6), EIS of ZIF-8, CNTs and ZnO@CNT (Fig. S7(a)), ZnO@CNT load model (Fig. S7(b)), the carbon nanotube HOMO diagram (Fig. S7(c)), the ZnO@CNT HOMO diagram (Fig. S7(d)), potential adsorption models of PDS molecules on ZnO@CNT (Fig. S8), the degradation mechanism of SMX in the ZnO@CNT/PDS system (Fig. S9), catalyst universality results (Fig. S10), and TOC removal rates (Fig. S11). See DOI: https://doi.org/10.1039/d6va00039h.

Acknowledgements

This study was supported by the National Natural Science Foundation of China (22402032).

References

1 Z. Liu, L. Ge, K. Wang, H. Yin, D. Li, S. Yang, G. Wang and D. Miao, Remediation of sulfonamides-contaminated groundwater through in-situ activation of peroxymonosulfate by supported hierarchical CuO/MgO nanosheets, *J. Water Proc. Eng.*, 2023, **53**, 103781.

2 J. Chen and S. Xie, Overview of sulfonamide biodegradation and the relevant pathways and microorganisms, *Sci. Total Environ.*, 2018, **640–641**, 1465–1477.

3 A. J. Browne, M. G. Chipeta, G. Haines-Woodhouse, E. P. A. Kumaran, B. H. K. Hamadani, S. Zaraa, N. J. Henry, A. Deshpande, R. C. Reiner Jr, N. P. J. Day, A. D. Lopez, S. Dunachie, C. E. Moore, A. Stergachis, S. I. Hay and C. Dolecek, Global antibiotic consumption and usage in humans, 2000-18: a spatial modelling study, *Lancet Planet. Health*, 2021, **5**, e893–e904.

4 Z. Wan and J. L. Wang, Degradation of sulfamethazine antibiotics using Fe3O4-Mn3O4 nanocomposite as a Fenton-like catalyst, *J. Chem. Technol. Biotechnol.*, 2017, **92**, 874–883.

5 G. S. Zhang, Y. Wang, M. Chen, J. X. Xu and L. Wang, ZIF-67-derived carbon@Co3S4/CoSO4/MnO polyhedron to activate peroxymonosulfate for degrading levofloxacin: Synergistic effect and mechanism, *Chem. Eng. J.*, 2023, **451**, 138976.

6 L. Zhang, S. Tian, Z. Tang, Y. Wang, S. Du and D. Cang, Exploration of sulfamethoxazole removal triggered by copper slag-based geopolymer: Radical versus nonradical contributions, *Chem. Eng. J.*, 2024, **496**, 154310.

7 J. Li, Y. Li, M. Chen, X. Tang, N. Zhu, W. Li, Q. Mei, S. Yue, Y. Tang and Q. Wang, Construction of polynary systems by coupling Cd/CdS with magnetic recyclable CuO/Fe2O3/CuFe2O4 nanocomposite for enhancing photo-Fenton degradation of antibiotics, *J. Environ. Chem. Eng.*, 2023, **11**, 111089.

8 L. Zhang, J. Zhang, F. Yang and Z. Chen, Exploring the impact of ultrasound on antibiotic-resistant bacteria inactivation in the sulfidated zero valent iron/persulfate system, *J. Environ. Chem. Eng.*, 2023, **11**, 109702.

9 L. Zhang, F. Yang, Z. Cang, J. Zhang, Z. Chen, C. Yu and Q. Wang, Insight into the degradation of sulfamethoxazole in novel persulfate activation system based on steel slag-based geopolymer, *J. Environ. Chem. Eng.*, 2023, **11**, 110095.

10 L. W. Matzek and K. E. Carter, Activated persulfate for organic chemical degradation: A review, *Chemosphere*, 2016, **151**, 178–188.

11 K. Zhi, D. Liu, J. Xu, Z. Li, S. Li, L. Luo, G. Gong, R. Han, A. Yin and L. Guo, N-doped graphene loaded with Ru sites as PMS activators for SMX degradation via non-radical pathway: efficiency, selectivity and mechanism, *Chem. Eng. J.*, 2025, **512**, 162230.

12 C. Gao, H. Ma, Z. Gao, X. Zhang and G. Wang, Ag nanoparticle anchored N-doped carbon nanotube photothermal catalytic membrane for high-efficiency water decontamination and fouling resistance, *J. Membr. Sci.*, 2025, **733**, 124341.

13 Z. Bahri, S. Djerad and L. Nouri, Oxidative Degradation of Basic Red 29 by Persulfate Activated by Sulfur Composite Zinc, *Phys. Status Solidi A*, 2022, **220**, 2200565.

14 D. A. Islam, G. M. Choudhury and H. Acharya, Layered double hydroxide (LDH)-derived zinc oxide (ZnO) nanorod on exfoliated graphene oxide (GO) nanosheet for photocatalytic dye degradation and hexavalent chromium reduction, *J. Solid State Chem.*, 2024, **336**, 124776.

15 C. B. Ong, L. Y. Ng and A. W. Mohammad, A review of ZnO nanoparticles as solar photocatalysts: Synthesis, mechanisms and applications, *Renewable Sustainable Energy Rev.*, 2018, **81**, 536–551.

16 W. Huang, S. Xiao, H. Zhong, M. Yan and X. Yang, Activation of persulfates by carbonaceous materials: A review, *Chem. Eng. J.*, 2021, **418**, 129297.

17 H. Lee, H. J. Lee, J. Jeong, J. Lee, N. B. Park and C. Lee, Activation of persulfates by carbon nanotubes: Oxidation of organic compounds by nonradical mechanism, *Chem. Eng. J.*, 2015, **266**, 28–33.

18 X. Cheng, H. Guo, Y. Zhang, G. V. Korshin and B. Yang, Insights into the mechanism of nonradical reactions of persulfate activated by carbon nanotubes: Activation

performance and structure-function relationship, *Water Res.*, 2019, **157**, 406–414.

19 Y.-G. Kang, H. Chi Vu, Y.-Y. Chang and Y.-S. Chang, Fe(III) adsorption on graphene oxide: A low-cost and simple modification method for persulfate activation, *Chem. Eng. J.*, 2020, **387**, 124012.

20 S. Wu, H. He, X. Li, C. Yang, G. Zeng, B. Wu, S. He and L. Lu, Insights into atrazine degradation by persulfate activation using composite of nanoscale zero-valent iron and graphene: Performances and mechanisms, *Chem. Eng. J.*, 2018, **341**, 126–136.

21 J. Peng, Z. Wang, S. Wang, J. Liu, Y. Zhang, B. Wang, Z. Gong, M. Wang, H. Dong, J. Shi, H. Liu, G. Yan, G. Liu, S. Gao and Z. Cao, Enhanced removal of methylparaben mediated by cobalt/carbon nanotubes (Co/CNTs) activated peroxymonosulfate in chloride-containing water: Reaction kinetics, mechanisms and pathways, *Chem. Eng. J.*, 2021, **409**, 128176.

22 H. Lee, H.-J. Lee, J. Jeong, J. Lee, N.-B. Park and C. Lee, Activation of persulfates by carbon nanotubes: Oxidation of organic compounds by nonradical mechanism, *Chem. Eng. J.*, 2015, **266**, 28–33.

23 C. Wang, J. Kang, P. Liang, H. Zhang, H. Sun, M. O. Tadé and S. Wang, Ferric carbide nanocrystals encapsulated in nitrogen-doped carbon nanotubes as an outstanding environmental catalyst, *Environ. Sci.: Nano*, 2017, **4**, 170–179.

24 X. Shen, Y. Gao, X. Yuan, Q. Li, B. Li, X. Guo and X. Wang, Activation of peroxymonosulfate and peroxydisulfate by nitrogen-doped carbon nanotubes for effective degradation of neonicotinoid insecticides, *J. Environ. Chem. Eng.*, 2024, **12**, 113052.

25 Y. Shen, Q. Shen, C. Zhu, Y. Lin, Q. Fang, R. Liu, J. Wang, L. Lu and S. Song, Pyridinic nitrogen-modulated carbon nanotubes facilitate dual-electron transfer for polymerization-enhanced pollutant removal, *Appl. Catal. B Environ. Energy*, 2025, **378**, 125579.

26 Q. Wang, S. Yang, Y. Wu, O. Monfort and W. Dong, Nanoconfinement assists the selective generation of singlet oxygen to efficiently remove emerging organic contaminants in soil with a low consumption of oxidant, *J. Hazard. Mater.*, 2025, **497**, 139677.

27 X. Zhou, M.-K. Ke, G.-X. Huang, C. Chen, W. Chen, K. Liang, Y. Qu, J. Yang, Y. Wang, F. Li, H.-Q. Yu and Y. Wu, Identification of Fenton-like active Cu sites by heteroatom modulation of electronic density, *Proc. Natl. Acad. Sci. U. S. A.*, 2022, **119**, e2119492119.

28 C. Han, X. Duan, M. Zhang, W. Fu, X. Duan, W. Ma, S. Liu, S. Wang and X. Zhou, Role of electronic properties in partition of radical and nonradical processes of carbocatalysis toward peroxymonosulfate activation, *Carbon*, 2019, **153**, 73–80.

29 Z. Li, W. X. Jiang, J. W. Huang, Y. W. Wang and H. Guo, ZnO Promoted Persulfate Activation in Discharge Plasma System for Ofloxacin Degradation, *Catalysts*, 2023, **13**, 847.

30 G. Singla, S. N. Bhange, M. Mahajan and S. Kurungot, Facile synthesis of CNT interconnected PVP-ZIF-8 derived hierarchically porous Zn/N co-doped carbon frameworks for oxygen reduction, *Nanoscale*, 2021, **13**, 6248–6258.

31 M. Xu, H. Zhou, Z. Wu, N. Li, Z. Xiong, G. Yao and B. Lai, Efficient degradation of sulfamethoxazole by NiCo(2)O(4) modified expanded graphite activated peroxymonosulfate: Characterization, mechanism and degradation intermediates, *J. Hazard. Mater.*, 2020, **399**, 123103.

32 W. Hu, W. Tong, Y. Li, Y. Xie, Y. Chen, Z. Wen, S. Feng, X. Wang, P. Li, Y. Wang and Y. Zhang, Hydrothermal route-enabled synthesis of sludge-derived carbon with oxygen functional groups for bisphenol A degradation through activation of peroxymonosulfate, *J. Hazard. Mater.*, 2020, **388**, 121801.

33 D. Kim and K. Yong, Boron doping induced charge transfer switching of a C3N4/ZnO photocatalyst from Z-scheme to type II to enhance photocatalytic hydrogen production, *Appl. Catal., B*, 2021, **282**, 119538.

34 N. Zhang, E. P. Tsang, K. Wang, J. Fang, Y. Li, G. Zhou and Z. Fang, Iron-nitrogen co-doped carbon nanotubes decorated with Cu(2)O possess enhanced electronic properties for effective peroxymonosulfate activation, *Sci. Total Environ.*, 2021, **764**, 142813.

35 Z. He, H. Wang, M. Li, L. Feng, J. Niu, Z. Li, X. Jia and G. Hu, Amorphous cobalt oxide decorated halloysite nanotubes for efficient sulfamethoxazole degradation activated by peroxymonosulfate, *J. Colloid Interface Sci.*, 2022, **607**, 857–868.

36 X. Zheng, Z. Zhang, S. Meng, Y. Wang and D. Li, Regulating charge transfer over 3D Au/ZnO hybrid inverse opal toward efficiently photocatalytic degradation of bisphenol A and photoelectrochemical water splitting, *Chem. Eng. J.*, 2020, **393**, 124676.

37 H. Deng, X. Fei, Y. Yang, J. Fan, J. Yu, B. Cheng and L. Zhang, S-scheme heterojunction based on p-type ZnMn2O4 and n-type ZnO with improved photocatalytic CO2 reduction activity, *Chem. Eng. J.*, 2021, **409**, 127377.

38 K. B. Zhang, X. C. Liu, Y. Wang, G. Yang, Y. Zhu, C. Y. Jiang, Z. C. Pan, X. A. Liu and B. Xing, Degradation of Sulfamethoxazole by Activation of Persulfate Based on Nitrogen-Doped Mesoporous Carbon, *Water, Air, Soil Pollut.*, 2024, **235**, 162.

39 C. Liu, L. Y. Liu, X. Tian, Y. P. Wang, R. Y. Li, Y. T. Zhang, Z. L. Song, B. B. Xu, W. Chu, F. Qi and A. Ikhlaq, Coupling metal-organic frameworks and g-C3N4 to derive Fe@N-doped graphene-like carbon for peroxymonosulfate activation: Upgrading framework stability and performance, *Appl. Catal., B*, 2019, **255**, 117763.

40 H. Z. Wang, W. Q. Guo, R. L. Yin, J. S. Du, Q. L. Wu, H. C. Luo, B. H. Liu, F. Sseguya and N. Q. Ren, Biochar-induced Fe(III) reduction for persulfate activation in sulfamethoxazole degradation: Insight into the electron transfer, radical oxidation and degradation pathways, *Chem. Eng. J.*, 2019, **362**, 561–569.

41 C. T. Guan, J. Jiang, S. Y. Pang, J. Ma, X. Chen and T. T. Lim, Nonradical transformation of sulfamethoxazole by carbon nanotube activated peroxydisulfate: Kinetics, mechanism and product toxicity, *Chem. Eng. J.*, 2019, **378**, 122147.

42 R. R. Solís, O. Dinc, G. D. Fang, M. N. Nadagouda and D. D. Dionysiou, Activation of inorganic peroxides with magnetic graphene for the removal of antibiotics from wastewater, *Environ. Sci.:Nano*, 2021, **8**, 960–977.

43 Y. Feng, D. Lin, K. Yang and W. Wu, Desorption hysteresis of antibiotics on biochar produced at high temperature: The role of amine groups and amidation reaction, *Sci. Total Environ.*, 2024, **952**, 175998.

44 G. Geng, Y. Gao, Z. Zhang, K. Gao, W. Zhang and J. Song, Renewable and robust biomass waste-derived Co-doped carbon aerogels for PMS activation: Catalytic mechanisms and phytotoxicity assessment, *Ecotoxicol. Environ. Saf.*, 2021, **220**, 112381.

45 L. Rao, Y. Yang, L. Chen, X. Liu, H. Chen, Y. Yao and W. Wang, Highly efficient removal of organic pollutants via a green catalytic oxidation system based on sodium metaborate and peroxymonosulfate, *Chemosphere*, 2020, **238**, 124687.

46 R. Elshypany, H. Selim, K. Zakaria, A. H. Moustafa, S. A. Sadeek, S. I. Sharaa, P. Raynaud and A. A. Nada, Elaboration of Fe3O4/ZnO nanocomposite with highly performance photocatalytic activity for degradation methylene blue under visible light irradiation, *Environ. Technol. Innovation*, 2021, **23**, 101710.

47 X. Huang, Q. Liu, J. Zhu, Y. Gao, S. Fang and J. Bi, Trace Sulfur Accelerated Peroxydisulfate Activation Based on a ZIF-67-Derived Nanostructure for Carbamazepine Degradation, *ACS Appl. Nano Mater.*, 2022, **5**, 18307–18319.

48 A. C. G. Mantovani, L. T. Chendynski, A. Salviato, D. Borsato, V. T. Santana and E. Di Mauro, Monitoring free radicals formation in the biodiesel oxidation reaction via electronic paramagnetic resonance, *Fuel*, 2018, **224**, 255–260.

49 P. Zhai, H. Liu, F. Sun, T. Chen, X. Zou, H. Wang, Z. Chu, C. Wang, M. Liu and D. Chen, Carbonization of methylene blue adsorbed on palygorskite for activating peroxydisulfate to degrade bisphenol A: An electron transfer mechanism, *Appl. Clay Sci.*, 2022, **216**, 106327.

50 B. Dong, Y. Wu, X. Teng, Z. Zhuang, Z. Gu, J. Zhang, F. Xing and S. Hong, Investigation of the Cl− migration behavior of cement materials blended with fly ash or/and slag via the electrochemical impedance spectroscopy method, *Constr. Build. Mater.*, 2019, **211**, 261–270.

51 D. Liu, C. Chen, X. Wang, X. Sun, B. Zhang, Q. Zhao, Z. Li, Z. Shao, X. Wang, G. Cui and S. Pang, Enhanced Quasi-Fermi Level Splitting of Perovskite Solar Cells by Universal Dual-Functional Polymer, *Adv. Mater.*, 2024, **36**, e2310962.

52 P. Zhang, Y. Yang, X. Duan, Y. Liu and S. Wang, Density Functional Theory Calculations for Insight into the Heterocatalyst Reactivity and Mechanism in Persulfate-Based Advanced Oxidation Reactions, *ACS Catal.*, 2021, **11**, 11129–11159.

53 X. Pan and X. Bao, The Effects of Confinement inside Carbon Nanotubes on Catalysis, *Acc. Chem. Res.*, 2011, **44**, 553–562.

54 T. Blazek and W. Gorski, Oxidases, carbon nanotubes, and direct electron transfer: A cautionary tale, *Biosens. Bioelectron.*, 2020, **163**, 112260.

55 J. Ma, Y. Yang, X. Jiang, Z. Xie, X. Li, C. Chen and H. Chen, Impacts of inorganic anions and natural organic matter on thermally activated persulfate oxidation of BTEX in water, *Chemosphere*, 2018, **190**, 296–306.

56 S. Chen, L. Ma, Y. Du, W. Zhan, T. C. Zhang and D. Du, Highly efficient degradation of rhodamine B by carbon nanotubes-activated persulfate, *Sep. Purif. Technol.*, 2021, **256**, 117788.

57 X. Long, Z. Xiong, R. Huang, Y. Yu, P. Zhou, H. Zhang, G. Yao and B. Lai, Sustainable Fe(III)/Fe(II) cycles triggered by co-catalyst of weak electrical current in Fe(III)/peroxymonosulfate system: Collaboration of radical and non-radical mechanisms, *Appl. Catal., B*, 2022, **317**, 121716.

58 Z. Wang, J. Bao, J. Du, L. Luo, G. Xiao and T. Zhou, Sulfamethoxazole degradation by alpha-MnO(2)/periodate oxidative system: Role of MnO(2) crystalline and reactive oxygen species, *Environ. Sci. Pollut. Res. Int.*, 2022, **29**, 44732–44745.

59 K. Luo, Y. Shi, R. Huang, X. Wei, Z. Wu, P. Zhou, H. Zhang, Y. Wang, Z. Xiong and B. Lai, Activation of periodate by N-doped iron-based porous carbon for degradation of sulfisoxazole: Significance of catalyst-mediated electron transfer mechanism, *J. Hazard. Mater.*, 2023, **457**, 131790.

60 S. Yanan, X. Xing, Q. Yue, B. Gao and Y. Li, Nitrogen-doped carbon nanotubes encapsulating Fe/Zn nanoparticles as a persulfate activator for sulfamethoxazole degradation: role of encapsulated bimetallic nanoparticles and nonradical reaction, *Environ. Sci.: Nano*, 2020, **7**, 1444–1453.

61 J. Yao, X. Zeng and Z. Wang, Enhanced degradation performance of sulfisoxazole using peroxymonosulfate activated by copper-cobalt oxides in aqueous solution: Kinetic study and products identification, *Chem. Eng. J.*, 2017, **330**, 345–354.

62 H. Chen and J. Wang, Degradation of sulfamethoxazole by ozonation combined with ionizing radiation, *J. Hazard. Mater.*, 2021, **407**, 124377.